The Astrophysical Journal, 592:299–310, 2003 July 20

NEAR-INFRARED SYNCHROTRON EMISSION FROM CASSIOPEIA A

Jeonghee Rho
SIRTF Science Center, California Institute of Technology, MS 220-6, Pasadena, CA 91125;
rho@ipac.caltech.edu

Stephen P. Reynolds[1]
Harvard-Smithsonian Center for Astrophysics, 60 Garden Street, Cambridge, MA 02138

William T. Reach and Tom H. Jarrett
SIRTF Science Center/IPAC, California Institute of Technology, MS 220-6, Pasadena, CA 91125

Glenn E. Allen
Center for Space Research, Massachusetts Institute of Technology, 70 Vassar Street, Cambridge, MA 02139-4307

and

John C. Wilson[2]
Space Sciences Building, Cornell University, Ithaca, NY 14853
Received 2003 January 8; accepted 2003 February 28

ABSTRACT

Recent high-energy observations of Cassiopeia A suggest the presence of synchrotron radiation, implying acceleration of cosmic rays by young supernova remnants. We detect synchrotron emission from Cas A in the near-infrared using Two Micron All-Sky Survey (2MASS) and Palomar 200 inch (5.1 m) PFIRCAM observations. The remnant is detected in the J, H, and K_s bands using 2MASS: the K_s band is the brightest, H is moderate, and J is faint. In the J and H bands, bright [Fe II] lines (1.24 and 1.64 μm) are detected spectroscopically. The Palomar observations include K_s-continuum, narrowband 1.64 μm (centered on [Fe II]) and 2.12 μm [centered on H_2 (1–0)] images. While the narrowband 1.64 μm image shows filamentary and knotty structures, similar to the optical image, the K_s image shows a relatively smooth, diffuse shell, remarkably similar to the radio image. The H_2 image is identical to the K_s-continuum image, with surface brightness reduced as expected for the ratio of filter bandwidths, showing no contribution of H_2 lines to the K_s-band image. The broadband near-infrared fluxes of Cas A are generally consistent with, but a few tens of percent higher than, an extrapolation of the radio fluxes. The hardening to higher frequencies is possibly due to nonlinear shock acceleration and/or spectral index variation across the remnant. We show evidence of spectral index variation across Cas A using the "spectral tomography" technique. The presence of near-infrared synchrotron radiation requires the rolloff frequency to be higher than 1.5×10^{14} Hz, implying that electrons are accelerated to energies of at least $E = 0.3B_{\rm mG}^{-1/2}$ ergs, or 0.2 TeV. The morphological similarity in diffuse emission between the radio and K_s-band images implies that synchrotron losses are not dominant, or we would expect to see a greater concentration in knots. We also show that dust continuum is not significant in the near-infrared emission of Cas A. Our observations show unambiguous evidence that the near-infrared K_s-band emission of Cas A is from synchrotron emission by accelerated cosmic-ray electrons.

Subject headings: acceleration of particles — ISM: individual (Cassiopeia A) — supernova remnants
On-line material: color figure

1. INTRODUCTION

The origin of cosmic rays has been unclear since their discovery. It has been widely thought that their energy is derived from supernovae, which are naturally associated with particle acceleration because they are the primary energy input for interstellar gas. Shocks are thought to be primary acceleration sites of cosmic rays. Some evidence that cosmic-ray electrons are accelerated in supernova remnant (SNR) shocks has been recently found using X-ray and gamma-ray observations. SN 1006 is a notable example. Its X-ray emission shows featureless pectra in the limb, strong evidence that the emission is synchrotron radiation (Koyama et al. 1995). The detection of TeV gamma rays, probably cosmic-ray background photons upscattered by ~100 TeV electrons, strengthened the claim of synchrotron emission in SN 1006 (Tanimori et al. 1998). There are a few other SNRs, including G347.3−0.5 (Koyama et al. 1997; Slane et al. 1999) and G266.2−1.2 (Slane et al. 2001), that show featureless X-ray spectra, possibly due to synchrotron emission. Other examples of synchrotron emission are less clear, complicated by mixture with thermal emission, such as Cassiopeia A and RCW 86 (Allen et al. 1997; Borkowski et al. 2001; Rho et al. 2002).

However, even if synchrotron radiation commonly contributes to the X-ray emission of SNRs, it does so at a level below the extrapolation from radio frequencies, by factors of 3–100 for 14 Galactic SNRs (Reynolds & Keohane 1999) and 11 SNRs in the LMC (Hendrick & Reynolds 2001). That is, the electron distribution responsible for radio synchrotron emission must steepen at energies below 100 TeV

[1] Permanent address: Department of Physics, North Carolina State University, Raleigh, NC 27695.
[2] Current address: 255 Astronomy Building, University of Virginia, 530 McCormick Road, Charlottesville, VA 22903.

in all of those 25 cases. This is problematic if SNRs are to accelerate cosmic rays up to the slight steepening around 3000 TeV in the cosmic-ray ion spectrum known as the "knee." While relativistic electrons may be subject to radiative losses during the acceleration process, this should not be a problem for ions, so perhaps in all those cases electron acceleration is limited by losses, while ion acceleration invisibly extends to much higher energies. Alternatively, only certain remnants (for instance, much older and larger ones than in the Reynolds & Keohane 1999 study) may produce the highest energy cosmic rays. Another possibility is that a few remnants, such as Cas A, have very much stronger magnetic fields, increasing both the acceleration rate and the importance of losses so that the required steepening in the electron spectrum can be due to losses, while ion acceleration can extend to 10^{15} eV and beyond (Ellison et al. 1999). Perhaps Cas A is a "superaccelerator" of cosmic rays.

While the observed X-rays from Cas A fall below the radio extrapolation by a smaller factor than in any other Galactic SNR in the Reynolds & Keohane (1999) sample, this of course does not demonstrate that a portion of those X-rays is due to synchrotron emission. Most of the soft X-rays (below 7 keV) are clearly thermal (see, e.g., Gotthelf et al. 2001), but emission is seen up to energies greater than 10 keV (Allen et al. 1997) with the *Rossi X-Ray Timing Explorer* (*RXTE*) and up to ~100 keV with OSSE on the *Gamma-Ray Observatory* (The et al. 1996). The latter study shows a power-law photon index of -3.1 ± 0.4. A spectrum this hard to such high energies cannot be produced by synchrotron emission from shock-accelerated electrons in any reasonable model. The most likely explanation is nonthermal bremsstrahlung (NB; see, e.g., Asvarov et al. 1989; Laming 2001) from the lowest energy nonthermal electron population, the beginning of the distribution that extends up to radio-emitting electrons at around 1–10 GeV. Evidence for at least some X-ray synchrotron emission near shock fronts was reported by Gotthelf et al. (2001), but the total emission in the apparent synchrotron component is a small fraction of the total flux in the 4–6 keV range, and Bleeker et al. (2001) cite observations from *XMM-Newton* to assert only a small role for synchrotron emission in the total X-ray flux. Thus, the question of the highest frequency at which Cas A shows unambiguous synchrotron emission remains open.

Recently, a 5 σ detection of Cas A has been reported at gamma-ray energies above 1 TeV with the HEGRA Stereoscopic Cerenkov Telescope System (Aharonian et al. 2001). The emission could be due to leptonic processes (NB or inverse-Compton upscattering of cosmic microwave background photons) or hadronic (inelastic cosmic-ray proton collisions with ambient gas producing neutral pions that decay to gamma rays). NB would require electrons of energies of a few TeV; π^0-decay gamma rays would require similar energies for protons. Inverse-Compton emission from the cosmic microwave background, however, would indicate the presence of electrons of energies of the order of 100 TeV. However, until this detection is confirmed and the nature of the processes producing the gamma rays clarified, the highest particle energies present in Cas A are still uncertain.

The EGRET limits on emission above 100 MeV (Esposito et al. 1996) can be used to put a lower limit on the magnetic field strength of at least 0.4 mG (Atoyan et al. 2000); if the field were weaker, the required relativistic electron density would have to be higher to explain the radio emission, and those electrons would emit NB at levels higher than the upper limit in the EGRET band. Thus, Cas A seems to have a much larger magnetic field than those inferred for other remnants (e.g., ~10 μG for SN 1006; Tanimori et al. 1998; Dyer et al. 2001).

The total flux of Cas A at millimeter wavelengths (Liszt & Lucas 1999; Mezger et al. 1986) lies very close to the extrapolation from centimeter wavelengths. Shortward of 1.2 mm, however, there is very little information. Synchrotron continuum is required to fit the mid-infrared ISOCAM and *ISO* SWS (6–30 μm) spectra, and the spectral shape of synchrotron emission (i.e., a power law) dominates between 6 and 8 μm (Douvion, Lagage, & Pantin 2001, hereafter DLP01). Tuffs et al. (1997) suspected from *ISO* data that emission in a line-free region near 6 μm could be synchrotron. Gerardy & Fesen (2001) report that a *K*-band image resembles the radio but give no quantitative flux determinations. Here we search for synchrotron emission from Cas A in the infrared and show a definitive detection of synchrotron radiation at near-infrared wavelengths. We discuss the implications of our result for theories of particle acceleration and cosmic-ray origin in supernova remnants.

2. OBSERVATIONS AND RESULTS

2.1. *2MASS*

The images of Cas A were obtained as part of the routine observations for the Two Micron All Sky Survey (2MASS; Skrutskie et al. 1997; Cutri et al. 2002[3]) using the northern telescope at Mount Hopkins, Arizona, on 1998 December 26. The wavelength coverages of the bands are 1.11–1.36 μm (J), 1.5–1.8 μm (H), and 2–2.32 μm (K_s). The spatial resolution of 2MASS is 3″. The detailed calibration of diffuse emission is explained in Rho et al. (2001). Here we used updated zero-point fluxes of 1592, 1024, and 668.8 Jy for J, H, and K_s, respectively. Figure 1 shows the 2MASS three-color image of Cas A, revealing a shell-like morphology for the near-infrared emission. The K_s- and H-band images are brighter than the J-band image, and the J-band emission is barely detected in 2MASS. The differences in morphology among the three bands are not very noticeable, except in the southwestern shell. The three-color image in Figure 1 contrasts the difference: K_s emission (reddish in color) dominates for most of Cas A, and H-band emission (greenish in color) is more noticeable in the southwestern shell, some inner parts of the northern shell, and sparsely distributed knots.

We obtained a few near-infrared spectra of Cas A using the CorMASS instrument (Wilson et al. 2001) on the Palomar 60 inch (1.5 m) telescope. The observations took place on 2000 September 10–12 and November 14–15. The CorMASS spectra toward the northwestern and southwestern shells show bright lines of [Fe II] in the J and H bands (at 1.26 and 1.64 μm), which is consistent with the spectra of Gerardy & Fesen (2001), and no lines in the K_s band were detected. We also took the spectra toward possibly synchrotron-dominated positions (positions D and C in Hughes et al. 2000, where no or weak X-ray emission lines are detected), and the [Fe II] was not detected from these

[3] See http://www.ipac.caltech.edu/2mass.

FIG. 1.—Mosaicked 2MASS three-color atlas image of Cas A. The color ranges are 0.7–3.7 μJy (*J*, *blue*), 5–29 μJy (*H*, *green*), and 7–38 μJy (K_s, *red*) per 1″ pixel. Most of the diffuse emission is K_s band–dominated, but there are a few places showing significant *H*-band emission, in particular, in the southwestern shell. The position of the center is ($23^h23^m25\overset{s}{.}7$, $58^\circ48'52''$ [J2000.0]), and the image size is 12′.

positions. This indicates that the line-emitting region is spatially limited across the remnant. The line contribution to each filter is estimated based on the near-infrared spectra from Gerardy & Fesen (2001), which is described in § 3.1.

2.2. *Palomar 200 inch PFIRCAM Images*

We observed Cas A on 2001 July 12–13 using the Prime Focus Infrared Camera (PFIRCAM) on the Hale 200 inch (5.1 m) telescope on Palomar Mountain. The PFIRCAM has a 256 × 256 pixel array, with a pixel scale of 0.″494 at the f/3.3 prime focus of the 200 inch telescope. We took K_s broadband ($\Delta\lambda = 0.32$ μm), [Fe II] narrow-filter ($\lambda = 1.64$ μm, $\Delta\lambda = 0.016$ μm), and H_2 ($\lambda = 2.12$ μm, $\Delta\lambda = 0.02$ μm) images. Our goal was to distinguish the structures between the line and continuum as well as to measure the remnant fluxes. The seeing was 1″–1.″5. We used the observational technique described in Reach et al. (2002).

The integration times per sky pixel for the K_s, Fe II, and H_2 images are 30, 60, and 60 s, respectively. The PFIRCAM images were calibrated by comparing photometry of sources in the field to the 2MASS catalog (Cutri et al. 2002[4]). The K_s

[4] See footnote 3.

image was calibrated using 68 stars with 2MASS K_s magnitudes ranging from 12.5 to 14.5, the H_2 image was calibrated using 43 stars with 2MASS K_s magnitudes ranging from 11.0 to 14.5, and the [Fe II] image was calibrated using 52 stars with 2MASS H-band magnitudes ranging from 12.6 to 14.6. Bright stars were excluded from the fit because of nonlinearity in the PFIRCAM data; the diffuse emission is equivalent to stars fainter than 18 mag and is well within the linear regime of the detector. The total remnant fluxes were measured from the near-infrared images after subtracting stars using the DAOPHOT package. The regions (9″ radius) of two bright stars in the west were excluded from the estimation of the total fluxes.

The narrowband mosaicked image of [Fe II] in Figure 2 (*blue*) is globally similar to the optical image (DLP01; Fesen, Becker, & Blair 1987), showing sharp filamentary and knotty structures of Fe-rich ejecta. However, while [Ne] and [S II] optical maps show brighter emission in the north,

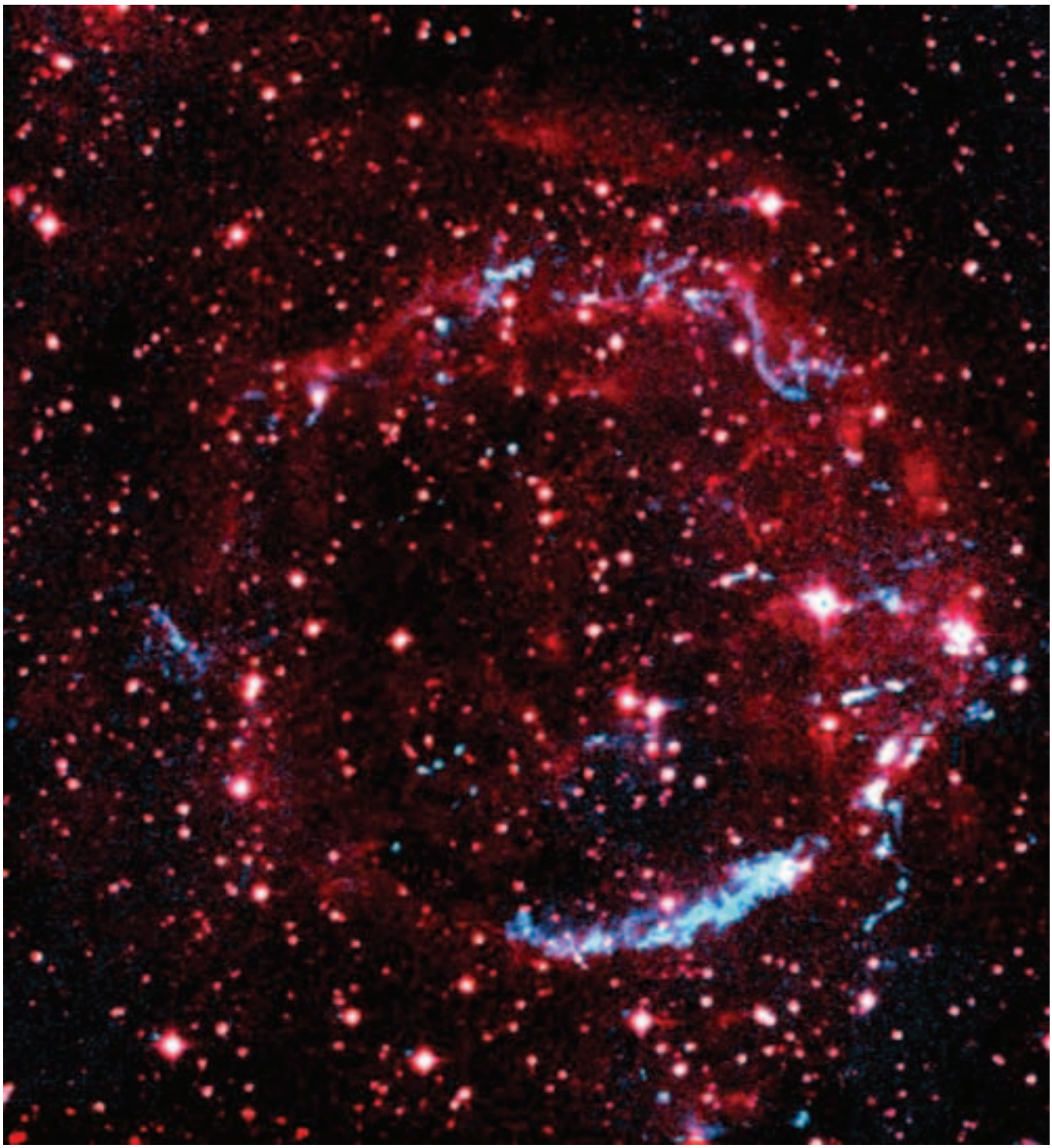

FIG. 2.—Mosaicked Palomar PFRICAM two-color images of K_s (*red*) and [Fe II] (*blue*). The narrowband [Fe II] image shows filamentary and knotty structures (from ejecta material) that are not present in the broadband K_s image, which is dominated by synchrotron emission. The colors are 5–82 μJy (*blue*) and 2–11 μJy (*red*) per 0.″5 pixel. The center of the image is the same as in Fig. 1, and the image size is 6.′4.

the [Fe II] image shows much brighter emission in the southwest.

Figures 2 (*red*) and 3*a* show the Palomar PFIRCAM K_s-band image, which is noticeably different from the Fe II–band image. The K_s-band structure is much smoother than the ejecta structure that dominates the [Fe II] and optical images. The H_2-band image is essentially identical to the K_s image, with surface brightness reduced (and noise increased) as expected for the ratio of filter bandwidths; thus, the H_2 band appears to be completely due to the same continuum that generates the K_s-band image. We show the 1.4 GHz radio image (Anderson et al. 1991) in Figure 3*b* for comparison with the K_s-band image, because they are remarkably similar. The radio image of Anderson et al. (1991) has a pixel size of 0.″4 and a spatial resolution of 1.″3, which is comparable to our Palomar image. The similarity between the K_s-band and radio images suggests that both the K_s and radio images are due to the same physical process: synchrotron radiation.

3. INFRARED FLUX OF CAS A

3.1. *Total Flux from Near-Infrared Images*

The total remnant flux from the PFIRCAM K_s-band image is 0.32 ± 0.03 Jy, where the error includes the uncertainty in calibration. In comparison, the 2MASS flux in the K_s band is 0.31 ± 0.02 Jy. Although the 2MASS diffuse

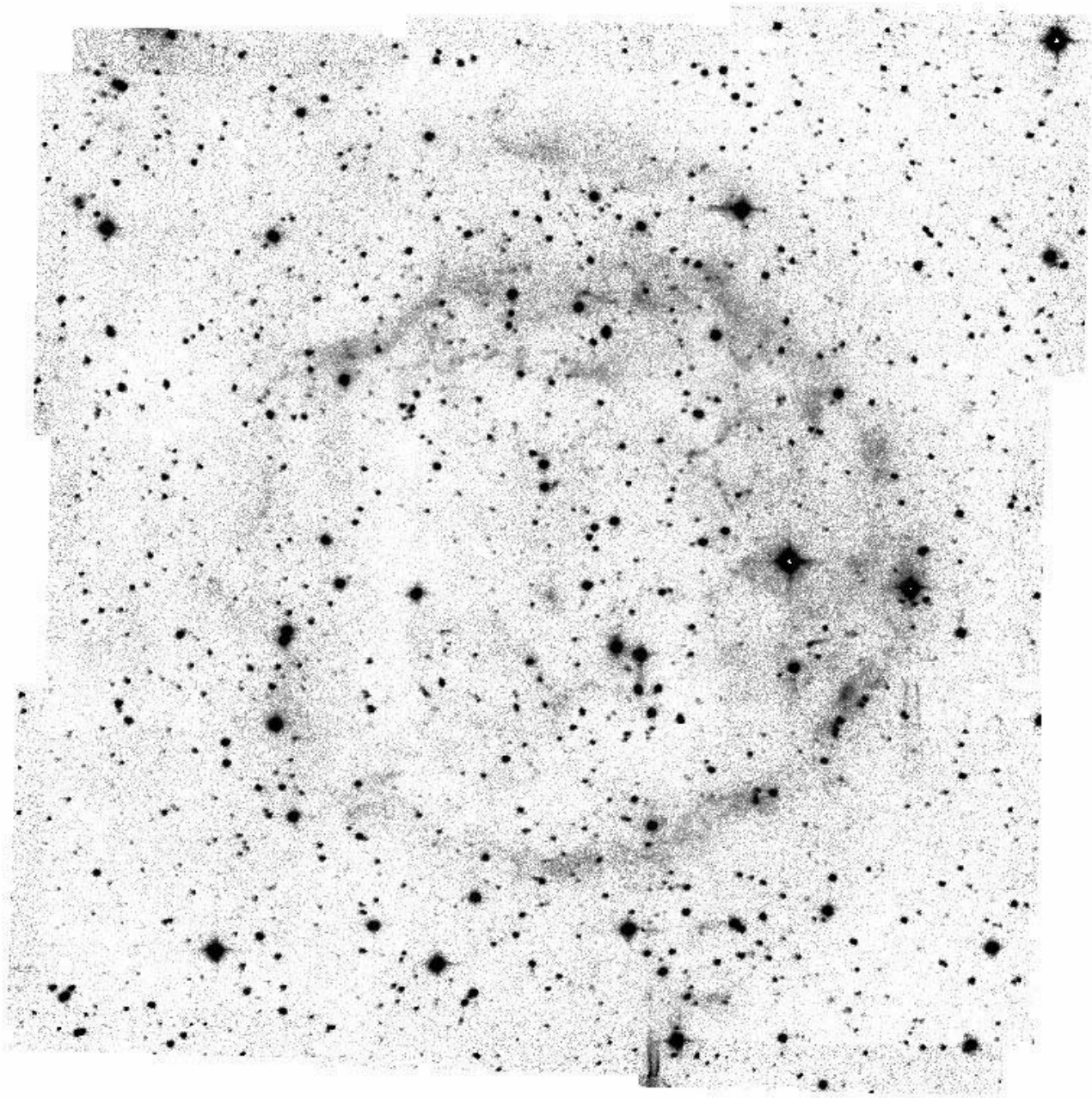

FIG. 3*a*

FIG. 3.—(*a*) K_s-band image of Cas A. (*b*) Radio image of Cas A at 1.4 GHz (Anderson et al. 1991). The K_s and radio images are remarkably similar, except of course for the presence of unrelated stars in the K_s image. [*See the electronic edition of the Journal for a color version of this figure.*]

FIG. 3*b*

emission may include some faint stars because of lower spatial resolution, the K_s-band flux is consistent between PFIRCAM and 2MASS. The statistical errors of the measurement are less than 1%, but a larger error is induced by the method of star subtraction because sometimes the sampling of the fluxes for the stars is insufficient or it is unclear if the bright blobs are faint stars or diffuse emission, especially in the [Fe II] image. We experimented with different thresholds of star identification, and we believe the error would not be larger than 20% of the measured flux (a conservative estimate). Extinction varies across the remnant, with A_v ranging typically from 4.3 to 6.2 mag (Searle 1971; Fesen et al. 1987) and as high as 8 mag in the western boundary (Hurford & Fesen 1996). The extinction-corrected K_s flux is $0.53^{+0.12}_{-0.04}$ Jy, using the near-infrared extinction law of Rieke & Lebofsky (1985); the error includes the possible range of extinction. The CorMASS spectra show no lines in the K_s band, and Gerardy & Fesen (2001) also detected no lines within the K_s band (2–2.3 μm) from fast-moving knot (FMK) positions in the north and northeast of the remnant, while they detected faint lines of [Fe II], He I, and H II Brγ from quasi-stationary flocculum (QSF) positions in the southwest. It is likely that the line contribution is very small in the K_s-band image, considering that (1) QSF covers a small portion of the remnant, (2) the morphology of the K_s image is remarkably similar to that of the radio image, and (3) the narrow-filter 2.12 μm image is very similar to the K_s-band image.

The total flux of the PFIRCAM [Fe II] image is 0.37 ± 0.06 Jy, and the extinction-corrected flux is 0.76 Jy using an A_v of 4.5 mag. This total flux is somewhat uncertain, because the [Fe II] emission is knotty and filamentary and some of the bright peaks of diffuse emission may have been subtracted during subtraction of stars. The 2MASS total flux in the H band is 0.27 Jy, and the extinction-corrected flux is 0.56 Jy. The 2MASS H-band flux may be

somewhat overestimated because of contribution from unresolved faint stars. Experimenting with different star-subtraction methods shows that neither of these effects are significant.

Emission lines contribute a small fraction of the flux observed in the wide K_s band. We estimate the line contribution as follows. We assume that the emission in each band arises from a combination of a featureless continuum and spectral lines, with a total brightness in the H band that is a factor f_L brighter than the [Fe II] 1.64 μm line. Using the observed fluxes and the filter widths, the line contribution to the H band is $\sim 2f_L\%$, and even in the narrow [Fe II]–centered filter, it is only $\sim$30% because of the 1.64 μm line. Spectroscopically, the 1.64 μm line is the dominant line in the H band, as found in observations by Gerardy & Fesen (2001) from FMK positions. While the 1.64 μm line is dominant ($f_L \simeq 1$) from FMK positions, the QSFs have a wide range of lines, with $f_L \sim 2$. Thus, the H band is dominated by continuum emission, with lines contributing less than 4% of the in-band flux. In the K_s band, the conclusion is even more clear, because of the paucity of spectral lines. For most positions, there are no spectral lines detected in the K_s band (in our CorMASS data and the FMK positions from Gerardy & Fesen 2001). Even using the line-rich QSF spectra, the total line brightness in the K_s band is 10% of the total line brightness in the H band, and spectral lines would contribute less than 1% of the K_s-band flux. The conclusion that continuum dominates the wide bands is robust, and even after accounting for the uncertainties from star-subtraction methods, the line contribution would be less than 8% in the H band and less than 2% in K_s band.

Measuring the J-band flux was challenging because 2MASS barely detected the diffuse emission from the remnant. The 2MASS J-band flux is 0.12 Jy, and the extinction-corrected flux is 0.39 Jy using an A_v of 4.5 mag, which may be highly uncertain. Gerardy & Fesen (2001) show a higher resolution J-band image, which is similar to our [Fe II]–band image. Their J-band spectra show a number of bright lines, such as [Fe II], [S II], and [P II], such that the total flux of lines in the J band is 7–9 times greater than in the H band. Using the line fraction derived above for the H band, we estimate that lines contribute $\sim$20%–40% of the J-band flux. The reason that the J-band and the narrow Fe-band images are similar is that they contain similar fractions of line emission.

3.2. *Possible Dust Contribution to Cas A Flux*

The mid-infrared spectrum of Cas A revealed dust newly formed from the ejecta material, as well as gas lines (DLP01). A model for the mid-infrared spectrum using dust composed of pyroxene, quartz, and aluminum oxide, with cold (90 K) and warm (350 K) components, can reasonably approximate the spectrum longward of 8 μm (DLP01). We estimated the dust contribution to the near-infrared brightness by calculating the ratio of the 2.2–8 μm brightness of small pyroxene (Dorschner et al. 1995) particles at 350 K, then scaling to the observed 8 μm brightness (DLP01). In Figure 3 of DLP01 it is evident that dust dominates at 8 μm and above and that the synchrotron component only begins to contribute significantly at 6 μm. We find that the synchrotron emission is 3–4 orders of magnitude higher than in the extrapolated dust model at 2.2 μm. We also estimated the brightness of starlight scattered by the Cas A dust, using the interstellar radiation field (Mathis, Mezger, & Panagia 1983), an albedo of 0.6, and the same optical depth as inferred from the mid-infrared thermal emission model (mostly from the colder component). The scattering contribution is 4–5 orders of magnitude smaller than that of synchrotron emission. Therefore, at 2.2 μm, synchrotron emission dominates over dust emission and scattering. Recent submillimeter observations of Cas A show that no dust is present at 850 μm (Loinard et al. 2003), which strengthens our conclusion of no dust contribution at 2 μm.

4. NEAR-INFRARED SYNCHROTRON RADIATION FROM CAS A

We show the broadband spectrum of Cas A, from radio to TeV energies, in Figure 4. The data from Baars et al. (1977) for 10–35 MHz, Liszt & Lucas (1999) for 86 and 140 GHz, and Mezger et al. (1986) for 1.2 mm are marked. The high-energy data of *RXTE* (Allen et al. 1997), OSSE (The et al. 1996), EGRET (Esposito et al. 1996), and Whipple (Lessard et al. 1995) are also indicated. Our near-infrared points are above the fit to the radio data (*solid line*) with $\alpha = -0.77$ (where $\log S = \beta + \alpha \log \nu$, $\beta = 5.745 \pm 0.025$ for ν in MHz [Baars et al. 1977], which is equivalent to $\beta = 10.365$ for ν in Hz). This shows that the K_s flux before correcting for extinction is comparable to the lower frequency extrapolation and that the extinction-corrected K_s flux is $\sim$70% higher than that extrapolation. When we performed a weighted fit to the radio, millimeter, and near-IR data, we obtain an index that is not significantly different from -0.77, and the value of the constant β is sightly higher than that in Baars et al. (10.409 ± 0.029; see the thick solid line in Fig. 4). The extrapolation of this spectrum fell below the near-IR data points, suggesting positive (concave-up) curvature. An index flatter than -0.77 has been suggested by Mezger et al. (1986); they found -0.65. When we fit the

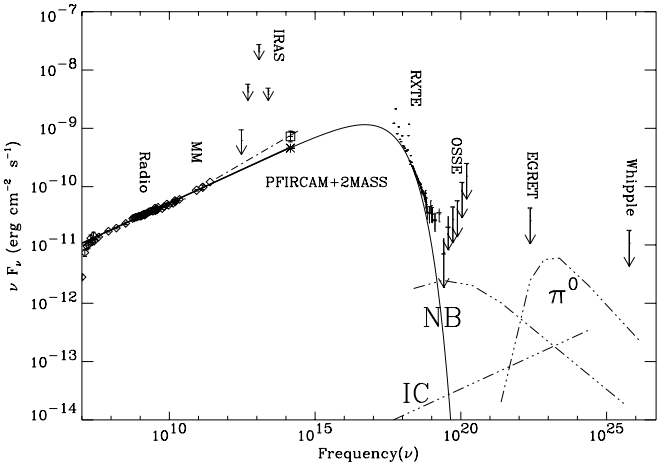

FIG. 4.—Broadband frequency and flux spectrum of Cas A. The near-infrared K_s flux is marked with an asterisk, and the extinction-corrected flux is marked as a square (assuming $A_v = 4.5$ mag). The solid line shows a spectral index of -0.77, which is derived using all the radio, near-IR, 86 GHz, and 140 GHz fluxes, with an exponential cutoff applied. The dot-dashed line shows a spectral index of -0.71, which is derived using only the near-IR, 86 GHz, and 140 GHz fluxes. The double-dot–dashed lines show nonthermal-bremsstrahlung (NB), inverse-Compton scattering of the cosmic microwave background (IC), and the decay of neutral pions (π^0) from Allen et al. (1997).

86 GHz, 140 GHz, 1.2 mm, and 2 μm data alone, $\alpha = -0.709 \pm 0.040$ and $\beta = 9.762 \pm 0.444$, showing a hardening to higher frequencies, although we cannot completely rule out the possibility that the excess near-IR flux above the extrapolation is due to contamination from line emission.

It is possible that the concave spectrum between 140 GHz and the near-IR is at least partially due to spectral index variations across the remnant. If different shocks produce slightly different spectral indices, perhaps because of differences in Mach number, shocks with harder spectra will come to dominate at higher frequencies, and the spatially integrated spectrum will be concave. Spectral-index variations between 1.4 and 5 GHz were studied by Anderson et al. (1991), who obtained values from -0.64 to -0.92. Figure 5 is a two-color image with the radio image (1.4 GHz; Anderson et al. 1991) in red and the star-subtracted K_s-band image in green, and it shows spectral index variations. Radio-dominated regions (red in Fig. 5) have a steeper spectral index, and K_s band–dominated regions (green in Fig. 5) have a flatter spectral index between the radio and K_s frequencies. The noticeable steep spectral index regions (red in Fig. 5) are the southeastern shell and knots and a blob in the west outside of the shell (at R.A. = $23^{h}23^{m}8^{s}.5$, decl. = $58^{\circ}48'44''$ [J2000.0]). By contrast, the southwestern rim appears to have a relatively flat spectrum. This image is indeed very similar to the radio spectral index map between 1.4 and 5 GHz, which is shown in Figure 3 of Anderson et al. (1991). Figure 6 shows K_s-band and radio radial profiles averaged over 5°–10° sectors toward the north, northeast, southeast, and southwest directions (each position angle is given in the figure

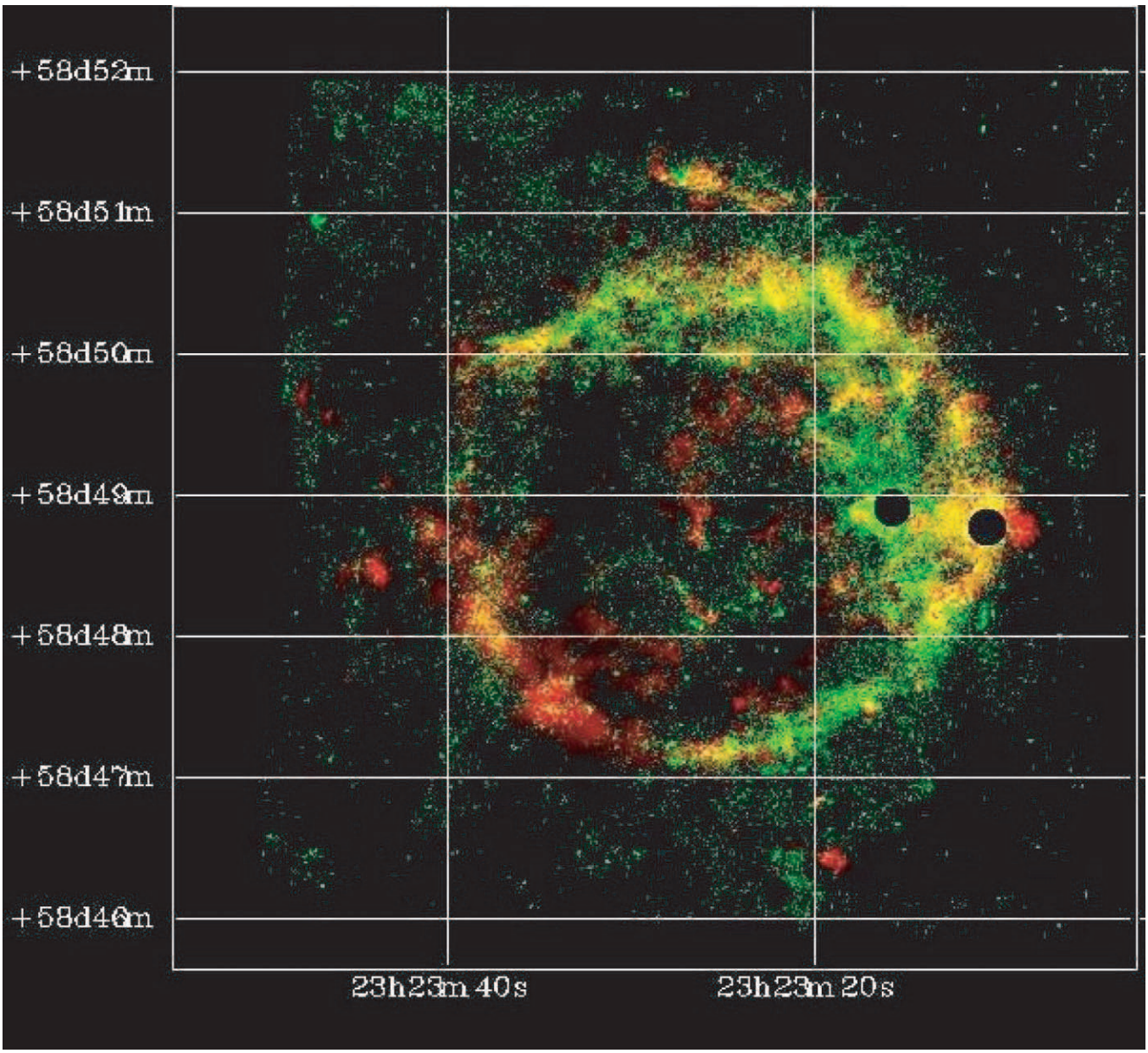

FIG. 5.—Two-color images of the K_s band (*green*) and radio (*red*). Stars have been subtracted from the K_s-band image. The area emitting in both the K_s band and radio appears in yellow. The three saturated stars are masked. This image highlights differences between the K_s and radio emission from the remnant, with the southeast being relatively radio-bright.

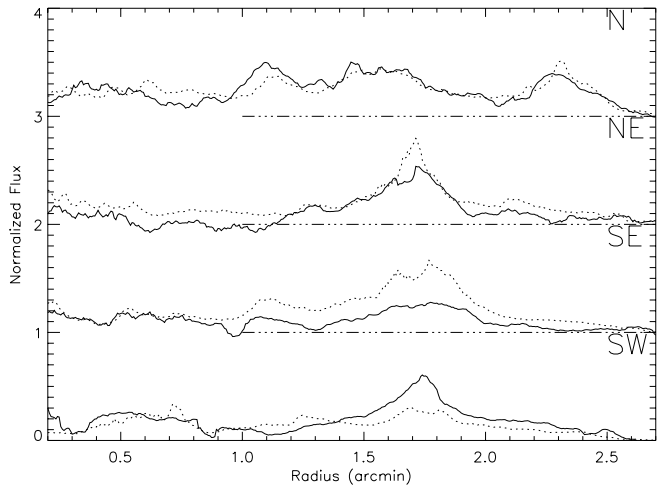

FIG. 6.—Radial profiles of K_s-band (*solid lines*) and radio (*dashed lines*) images. We chose the center position of R.A. = $23^h23^m26^s$, decl. = 58°48′42″ (J2000.0); north covers position angles (eastward from the north) of 355°–360°; northeast covers P.A. of 45°–50°; southeast covers P.A. of 135°–145°; southwest covers P.A. of 210°–220°. The relative fluxes are conserved within each K_s and radio image.

caption). While the K_s-band and radio profiles are similar in the north and northeast (except that the radio is more sharply peaked in the shell), the K_s image is noticeably fainter in the southeastern shell and brighter in the southwestern shell, which is consistent with what we see in Figure 5.

We have also constructed images using the "spectral tomography" technique (Katz-Stone & Rudnick 1997), in which scaled versions of one image are subtracted from another. That is, for a series of trial values $\alpha_t(<0)$, we subtract from the radio image the K_s-band image multiplied by $(\nu_{\rm radio}/\nu_{\rm IR})^{\alpha_t}$. In such images, emission with a spectrum steeper than α_t appears positive, while flatter spectrum emission appears negative. In Figure 7, we show images for $\alpha_t = -0.61$, -0.67, -0.73, and -0.77. Since the -0.61 image is essentially all positive and the -0.77 image all negative, the radio–near IR spectral index of different regions in Cas A is bracketed by these values. For $\alpha_t = -0.67$ and -0.73, we see both positive and negative structure. The disappearance of much of the emission along the bright southwestern and northern rims in the -0.67 image indicates that the average radio–near IR spectral index in these regions is about -0.67. Similarly, the southeastern rim mostly vanishes in the -0.73 image, showing that the average spectral index along the southeastern rim is about that value. These results are consistent with the two-color radio/K_s image, in which the southeastern rim appears steeper, while most of the rest of the remnant is flatter. There is a great deal of other small-scale structure in these images, whose more detailed investigation might provide useful information on the location and properties of electron acceleration.

However, it is not clear that the observed integrated spectrum concavity can be produced by simply adding contributions from regions with straight spectra with different slopes. For instance, a region with a 1.4–5 GHz radio spectral index flatter than the average by 0.13 would be about 5 times brighter at the K_s band than a region of comparable brightness at 1.4 GHz with the average spectrum. Such large variations do not appear to be the case. But another explanation for the concavity is available. Such concave-up curvature of the spectrum is predicted by nonlinear shock acceleration models in which shock transitions are broadened by preacceleration from cosmic rays diffusing ahead of the shock, if particles' diffusion lengths increase with energy. In this case, more energetic particles feel a higher velocity jump between upstream and downstream fluids, and the spectrum is flatter at those energies (Eichler 1984; Ellison & Reynolds 1991). Hints of this effect are seen in Tycho's and Kepler's SNRs (Reynolds & Ellison 1992) as well as in Cas A. If such concavity can be shown to be true for localized regions as well as for the spatially integrated spectrum, it will strongly support the case for such nonlinear effects. Other theories of particle acceleration, such as stochastic (second-order Fermi) acceleration in magnetohydrodynamic turbulence, predict a steepening spectrum (see, e.g., Cowsik & Sarkar 1984), so that our observation supports diffusive (first-order Fermi) shock acceleration instead. A recent paper by Jones et al. (2003) also showed the concavity of the spectrum from a small portion of the bright shell with the detection of polarized flux at 2.2 μm, which reinforces the concavity of the spectrum, i.e., the presence of nonlinear shocks in Cas A.

The synchrotron spectrum should eventually roll off because of one of several limitations on electron acceleration: radiative losses, finite acceleration time, or particle escape (Reynolds 1998; Sturner et al. 1997; Baring et al. 1999). For any of these, the electron distribution is likely to cut off no faster than exponentially (Reynolds 1998), with an e-folding energy $E_{\rm max}$. For a homogeneous source, the rolloff frequency is related to $E_{\rm max}$ by

$$\nu_{\rm rolloff} = 4.7 \times 10^{15} \frac{B_\perp}{\rm mG} \left(\frac{E_{\rm max}}{\rm TeV}\right)^2 \ {\rm Hz} \ ,$$

where $B_\perp$ is the sky plane component of the magnetic field. A lower limit for the rolloff frequency can be estimated directly from the high-frequency end of the K_s band, which is 1.5×10^{14} Hz. In a magnetic field B, synchrotron radiation at this frequency is produced by electrons with energies $E = 0.29 B_{\rm mG}^{-1/2}$ ergs, or ~0.2 TeV, where $B_{\rm mG}$ is the mean magnetic field in milligauss. These values assume that B lies entirely in the plane of the sky, since this gives us the most conservative lower limit on E. Our claim of the presence of electrons at these energies makes it more plausible that some portion of the X-ray emission is synchrotron as well.

Reynolds & Keohane (1999) obtained an upper limit to the rolloff frequency of 3.2×10^{17} Hz by assuming all the X-ray emission to be synchrotron. Since the X-ray emission obviously contains thermal emission with a rich line spectrum, this is a very conservative upper limit. Allen et al. (1997) used a cutoff frequency of 2.4×10^{17} Hz (1 keV). However, the cutoff frequency is very sensitive to the values of the spectral index from the radio.

The half-life of electrons with Lorentz factor γ radiating in a magnetic field B is given by

$$t_{1/2} = \frac{5.1 \times 10^8}{\gamma B^2} \ {\rm s} = 1.81 \times 10^{16} \nu^{-1/2} B_{\rm mG}^{-3/2} \ {\rm s} \ ,$$

where we have averaged over magnetic field directions. The electrons radiating in the K_s band ($\nu = 1.5 \times 10^{14}$ Hz) have lifetimes of only about $47 B_{\rm mG}^{-3/2}$ yr. With typical velocities in Cas A of several thousand kilometers per second, electrons in such strong fields could travel distances of the order of tens of arcseconds (for $d = 3.4$ kpc; Reed et al. 1995) in a

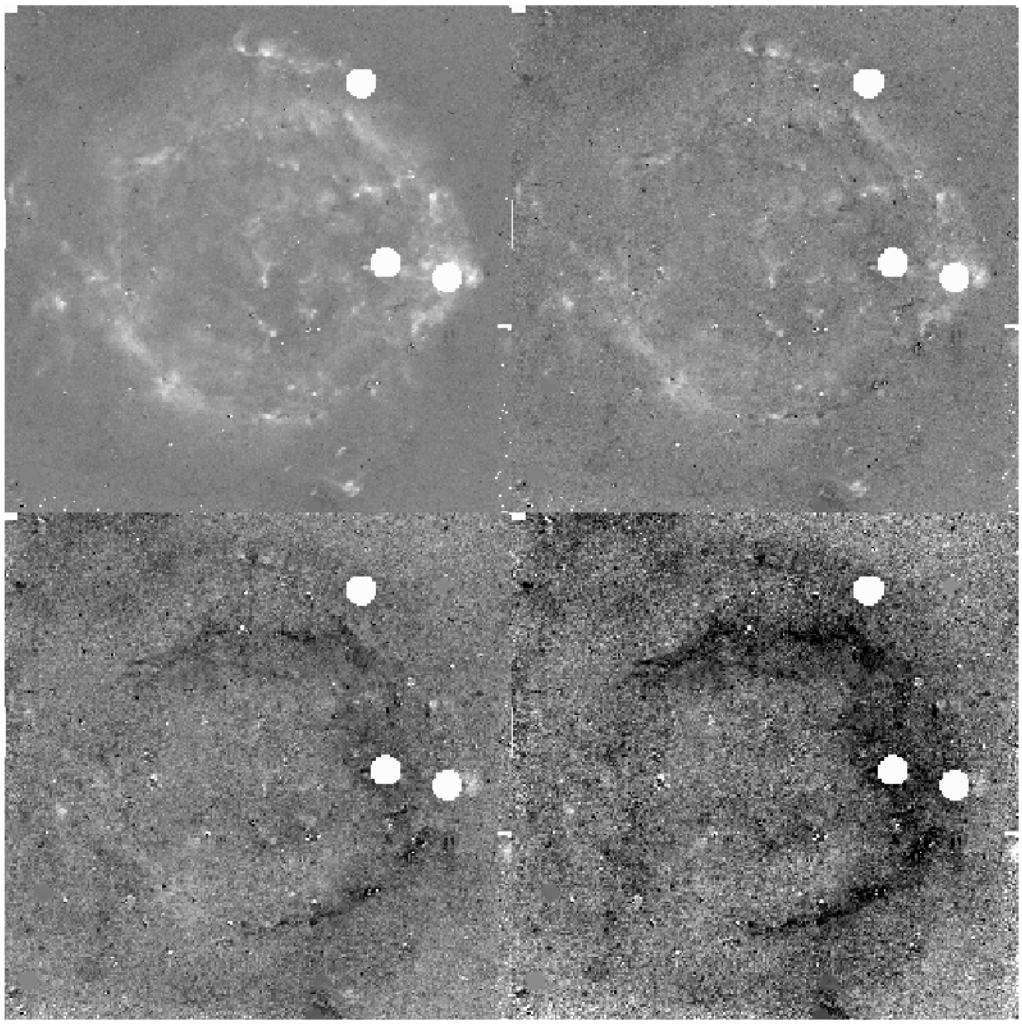

FIG. 7.—"Spectral tomography" maps: from the radio image we subtract the K_s-band image multiplied by $(\nu_{\rm radio}/\nu_{\rm IR})^{\alpha_t}$. White corresponds to positive values, softer (steeper) than the trial index, and dark to negative values, harder than the trial index. The scale is between −0.03 and 0.03. The three saturated stars are masked, shown in white. *Top left*: $\alpha_t = -0.61$; the spectral index is steeper than −0.61 for all of Cas A. *Top right*: $\alpha_t = -0.67$; the southwestern shell turns positive to negative. *Bottom left*: $\alpha_t = -0.73$; the northern shell and outer shock of northern shell change to negative. *Bottom right*: $\alpha_t = -0.77$; the only positive structure is the western edge knot. We deduce that the approximate spectral index is roughly −0.67 for the southwestern shell, roughly −0.73 for the northern shell and the upper part of southeastern shell, roughly −0.77 for the lower part of the southeastern shell, and steeper than roughly −0.77 for the western edge knot.

loss time. The synchrotron emissivity varies roughly as $n_{\rm els}B^{1+\alpha}$, where $n_{\rm els}$ is the energy density in relativistic electrons and α is the spectral index. If the magnetic field evolves by flux freezing and the relativistic electrons at these energies have relatively short diffusion lengths, we have $n_{\rm els}$ proportional to n, the thermal gas density and B proportional to a power of n between 0 and 1.8. Then the synchrotron emissivity varies as roughly n^2, like the optical emissivity; both optical emission and synchrotron emission would be prominent in high-density regions, showing that the morphological difference between the radio and optical is not due to density difference. The smoothness of the K_s-band and radio images, relative to optical images that more directly trace the shock fronts and high thermal gas densities, is due to the relatively large diffusion distances of the extremely high-energy synchrotron-emitting electrons, resulting in a generally smoother distribution of those electrons than that of thermal gas.

Even though the synchrotron loss time for the K_s band–emitting electrons is substantially less than the age of Cas A, it is much longer than the time required for shock acceleration to produce the electrons. We can estimate the acceleration time based on the general expression in Forman & Morfill (1979), for the particular case of electron mean free path proportional to gyroradius, $\lambda_{\rm mfp} = \eta r_g$, with $r_g = E/eB$ for extreme relativistic electrons, and making other reasonable assumptions detailed in Reynolds (1998). The acceleration time for parallel shocks (shock normal parallel to the upstream magnetic field) is

$$\tau_{\rm acc} = 1.3\eta(B_{\rm mG})^{-1}u_8^{-2}E \text{ yr} ,$$

where u_8 is the shock speed in units of 10^8 cm s^{-1} and E is in ergs. For perpendicular shocks, in which we assume a compression ratio of 4, the acceleration time is

$$\tau_{\rm acc} = 0.53\eta^{-1}(B_{\rm mG})^{-1}u_8^{-2}E \text{ yr} .$$

We infer that shocks can produce the K_s band–emitting electrons in times of the order of 1 yr. This very short timescale suggests that variability in acceleration, if not depletion, of

these electrons could be observed over timescales of the same order. Now the radio morphology of Cas A makes it clear that there is no single acceleration site like the outer shock wave in SN 1006; instead, particle acceleration appears to take place in many small knots all over the remnant (Anderson et al. 1991). This picture can be supported by detailed theoretical analysis (Atoyan et al. 2000). In the model of Atoyan et al. (2000), the magnetic field in the knots where acceleration takes place is much larger than that in the general remnant volume, so one would expect longer synchrotron lifetimes once electrons diffused out of the acceleration zones. In any case, to the extent that our K_s-band image resembles the radio, synchrotron losses are evidently not dominant, or we would expect to see less diffuse emission and a greater concentration in knots. But small differences between the images of Figure 5 show that it is not impossible that this greater concentration has already begun to occur.

While most authors agree that shock acceleration produces the relativistic electrons in Cas A, it is not impossible that some form of turbulent or stochastic acceleration is responsible (see, e.g., Cowsik & Sarkar 1984). One must ask if this mechanism, designed to describe radio emission, can in the time available produce the $\sim$1 erg electrons required by our near-infrared image. Melrose (1974) gives expressions for acceleration rates in magnetohydrodynamic turbulence that show that once electrons are substantially suprathermal ("injected," a necessity for shock acceleration as well), they can reach relativistic energies in a fraction of a year. Subsequent acceleration of relativistic electrons in MHD turbulence with amplitude $\delta B/B \equiv \epsilon$ takes place on a timescale

$$\tau_{\rm acc} \sim \frac{1}{\epsilon^2}\,\frac{r_g}{c}\left(\frac{v_{\rm A}}{c}\right)^{-2},$$

where $v_{\rm A}$ is the Alfvén speed and r_g is the electron's gyroradius. Strictly speaking, this result is true in the quasilinear approximation ($\epsilon \ll 1$), but it should provide at least a rough estimate for $\epsilon = 1$ to give us a conservative idea of the fastest possible acceleration. In the above expression, ϵ refers to the amplitude of waves resonant with the particular particle, which must be presumed to exist (perhaps generated by the particles themselves). Again assuming that the electron mean free path is a multiple of its gyroradius, $\lambda_{\rm mfp} \equiv \eta r_g$, quasilinear theory then gives $\eta = (\delta B/B)^{-2} = \epsilon^{-2}$, so we can rewrite the acceleration time as $\tau_{\rm acc} \sim (\lambda_{\rm mfp}/c)(v_{\rm A}/c)^{-2}$. Since in the extreme relativistic limit, $r_g = E/eB$, with E the particle energy, the acceleration time to a particular energy is just proportional to that energy. For the strong fields we anticipate in Cas A, $v_{\rm A} = 2.2 \times 10^8 B_{\rm mG}(\mu n_{\rm H})^{-1/2}$ cm s^{-1}, where the matter density is $\rho = \mu m_p n_{\rm H}$. So $v_{\rm A}/c \sim 10^{-2}$, and with $r_g = 2 \times 10^{12} E B_{\rm mG}^{-1}$ cm, we estimate $\tau_{\rm acc} \sim 10^6$ s to reach energies adequate to produce infrared synchrotron radiation (in these strong fields)—comparable to the rate of shock acceleration. This can occur because the strong magnetic fields in Cas A can give Alfvén speeds comparable to the current, decelerated outer blast wave speed. So stochastic acceleration can certainly proceed rapidly enough to explain our observations. The spectrum produced by stochastic acceleration will depend on the properties of the turbulence, and it is not clear if the required remarkably flat, slightly hardening spectrum can in fact be produced. However, neither shock acceleration nor stochastic acceleration can be ruled out on the basis of acceleration time arguments.

5. SUMMARY AND CONCLUSIONS

The 2MASS near-infrared images reveal emission from Cas A in the J, H, and K_s bands. The images reveal a shell-like morphology shown in Figure 1. The K_s- and H-band images are brighter than the J-band image. The three-color image demonstrates the difference: K_s emission is dominant for the majority of Cas A, and H emission is noticeable in the southwestern shell. Near-infrared spectra showed [Fe II] lines in J (1.25 μm) and H (1.64 μm), and no lines were detected within the K_s band.

A high-resolution Palomar PFIRCAM narrowband image of [Fe II] (1.64 μm) (see Fig. 2) is similar to the optical image of Cas A, showing sharp filamentary and knotty structures of Fe-rich ejecta. The PFIRCAM K_s-band image is much smoother and more diffuse than the ejecta structure that dominates the optical images (and is present in the [Fe II] image). Instead, the K_s image is remarkably similar to the radio image of Cas A, suggesting that the physical mechanism that produces radio emission synchrotron radiation is also responsible for the K_s-band emission. We measure a total flux of Cas A in the K_s band of 0.32 ± 0.03 Jy, implying a flux of $0.53^{+0.12}_{-0.04}$ Jy after correcting for extinction. The spectral energy distribution of Cas A shows that the near-infrared flux is close to an extrapolation of the radio fluxes, supporting our interpretation of the near-IR flux as synchrotron radiation. The near-infrared K_s-band fluxes are actually a few tens of percent higher than an extrapolation of the radio fluxes. Such positive (concave-up) curvature of the spectrum (hardening to higher frequencies) is predicted by nonlinear shock acceleration models in which shock transitions are broadened by preacceleration from cosmic rays diffusing ahead of the shock, if particles' diffusion lengths increase with energy.

The synchrotron spectrum may roll off because of any of several possible limitations on electron acceleration, including radiative losses, acceleration time, or particle escape; this is measured as the rolloff frequency. Our near-infrared emission measurement gives us a lower limit to the rolloff frequency of 1.5×10^{14} Hz. Synchrotron radiation at this frequency is produced by electrons with energies $E = 0.3 B_{\rm mG}^{-1/2}$ ergs, or about 0.2 TeV, where $B_{\rm mG}$ is the mean magnetic field in milligauss. The synchrotron loss time for electrons radiating in the K_s band is only about $47 B_{\rm mG}^{-3/2}$ yr. The fact that such electrons can thus travel only distances on the order of tens of arcseconds implies that particle acceleration takes place in many sites all over the remnant. Our K_s-band image resembles the radio image, so synchrotron losses evidently do not dominate the small-scale structure. The acceleration timescale for electrons with energy high enough to produce the near-infrared emission from Cas A is of the order of a year (or less), so either shock or stochastic acceleration is rapid enough to accelerate electrons to the required energies.

Our results confirm that supernova remnants are high-energy cosmic-ray acceleration sites that can produce 0.2 TeV particles. We also show that near-infrared observations are a good tool to study synchrotron radiation and cosmic-ray acceleration in supernova remnants.

J. Rho thanks Pierre-Olivier Lagage for discussion on synchrotron emission from mid-infrared observation, which gave her strong motivation for this project.

REFERENCES

Aharonian, F. A., et al. 2001, A&A, 370, 112
Allen, G. E., et al. 1997, ApJ, 487, L97
Anderson, M. A., Rudnick, L., Leppik, P., Perley, R., & Braun, R. 1991, ApJ, 373, 146
Asvarov, A. I., Guseinov, O. Kh., Dogel, V. A., & Kasumov, F. K. 1989, Soviet Astron., 33, 532
Atoyan, A. M., Tuffs, R. J., Aharonian, F. A., & Völk, H. J. 2000, A&A, 354, 915
Baars, J. W. M., Genzel, R., Pauliny-Toth, I. I. K., & Witzel, A. 1977, A&A, 61, 99
Baring, M. G., Ellison, D. C., Reynolds, S. P., Grenier, I. A., & Goret, P. 1999, ApJ, 513, 311
Bleeker, J. A. M., Willingale, R., van der Heyden, K., Donnerl, K., Kaastra, J. S., Aschenbach, B., & Vink, J. 2001, A&A, 365, L225
Borkowski, K. J., Rho, J., Reynolds, S. P., & Dyer, K. K. 2001, ApJ, 550, 334
Cowsik, R., & Sarkar, S. 1984, MNRAS, 207, 745 (erratum 209, 719)
Dorschner, J., Begemann, B., Henning, T., Jäger, C., & Mutschke, H. 1995, A&A, 300, 503
Douvion, T., Lagage, P. O., & Pantin, E. 2001, A&A, 369, 589 (DLP01)
Dyer, K. K., Reynolds, S. P., Borkowski, K. J., Allen, G. A., & Petre, R. 2001, ApJ, 551, 439
Eichler, D. 1984, ApJ, 277, 429
Ellison, D. C., Goret, P., Baring, M. G., Grenier, I. A., & Lagage, P.-O. 1999, Proc. 26th Int. Cosmic-Ray Conf. (Salt Lake City), 3, 468
Ellison, D. C., & Reynolds, S. P. 1991, ApJ, 378, 214
Esposito, J. A., Hunger, S. D., Kanbach, G., & Sreekumar, P. 1996, ApJ, 461, 820
Fesen, R. A., Becker, R. H., & Blair, W. T. 1987, ApJ, 313, 378
Forman, M. A., & Morfill, G. E. 1979, Proc. 16th Int. Cosmic-Ray Conf. (Kyoto), 5, 328
Gerardy, C. L., & Fesen, R. A. 2001, AJ, 121, 2781
Gotthelf, E. V., Koralesky, B., Rudnick, L., Jones, T. W., Hwang, U., & Petre, R. 2001, ApJ, 552, L39
Hendrick, S. P., & Reynolds, S. P. 2001, ApJ, 559, 903
Hughes, J., Rakowski, C. E., Burrows, D. N., & Slane, P. O. 2000, ApJ, 528, L109
Hurford, A. P., & Fesen, R. A. 1996, ApJ, 469, 246
Jones, T. J., Rudnick, L., Delaney, T., & Bowden, J. 2003, ApJ, 587, 227
Katz-Stone, D. M., & Rudnick, L. 1997, ApJ, 488, 146
Koyama, J., Petre, R., Gotthelf, E. V., Hwang, U., Mastuura, M. Ozaki, M., & Holt, S. S. 1995, Nature, 378, 255
Koyama, K., et al. 1997, PASJ, 49, L7
Laming, J. M. 2001, ApJ, 546, 1149
Lessard, R. W., et al. 1995, in Proc. 24th Int. Cosmic-Ray Conf. (Rome), 2, 475
Liszt, H., & Lucas, R. 1999, A&A, 347, 258
Loinard, L., Lequeux, J., Tilanus, R. P. T., & Lagage, P. O. 2003, in Rev. Mexicana Astron. Astrofis. Ser. Conf. 15, Winds, Bubbles and Explosions, ed. S. J. Arthure & W. J. Henney (Mexico, DF: Inst. Astron., UNAM), 267
Mathis, J. S., Mezger, P. G., & Panagia, N. 1983, A&A, 128, 212
Melrose, D. B. 1974, Sol. Phys., 37, 353
Mezger, P. G., Tuffs, R. J., Chini, R., Kreysa, E., & Gemünd, H. P. 1986, A&A, 167, 145
Reach, W. T., Rho, J., Jarrett, T. H., & Lagage, P.-O. 2002, ApJ, 564, 302
Reed, J. E., Hester, J. J., Fabian, A. C., & Winkler, P. F. 1995, ApJ, 440, 706
Reynolds, S. P. 1998, ApJ, 493, 375
Reynolds, S. P., & Ellison, D. C. 1992, ApJ, 399, L75
Reynolds, S. P., & Keohane, J. W. 1999, ApJ, 525, 368
Rho, J., Dyer, K. K., Borkowski, K. J., & Reynolds, S. P. 2002, ApJ, 581, 1116
Rho, J., Jarrett, T. H., Cutri, R. M., & Reach, W. T. 2001, ApJ, 547, 885
Rieke, G. H., & Lebofsky, M. J. 1985, ApJ, 288, 618
Searle, L. 1971, ApJ, 168, 41
Skrutskie, M. F., et al. 1997, in The Impact of Large Scale Near-IR Sky Surveys, ed. F. Garzón (Dordrecht: Kluwer), 25
Slane, P., Gaensler, B. M., Dame, T. M., Hughes, J. P., Plucinsky, P. P., & Green, A. 1999, ApJ, 525, 357
Slane, P., Hughes, J. P., Edgar, R. J., Plucinsky, P. P., Miyata, E., Tsunemi, H., & Aschenbach, B. 2001, ApJ, 548, 814
Sturner, S. J., Skibo, J. G., Dermer, C. D., & Mattox, J. R. 1997, ApJ, 490, 619
Tanimori, T., et al. 1998, ApJ, 497, L25
The, L.-S., Leising, M. D., Kurfess, J. D., Johnson, W. N., Hartmann, D. H., Gehrels, N., Grove, J. E., & Purcell, W. R. 1996, A&AS, 120, 357
Tuffs, R. J., Drury, L., Fischera, J., Heinrichsen, I., Rasmussen, I., Russel, S., & Völk, H. J. 1997, in Proc. 1st *ISO* Workshop on Analytical Spectroscopy, ed. A. M. Heras, K. Leech, N. R. Trams, & M. Perry (ESA SP-419; Noordwijk: ESA), 177
Wilson, J. C., et al. 2001, PASP, 113, 227